Opto-Electronic Advances

CN 51-1781/TN ISSN (Print) 2096-4579 ISSN (Online) 2097-3993

Vacancy oscillating mode in amorphous binary oxide film by terahertz time domain spectroscopy

Huan Liu, Haiyun Huang, Heng Yu, Zhi Gong, Fei Yu, Zheng Zhang, Zhiyong Tan, Juncheng Cao, Haiyun Liu*, Kan-Hao Xue*, Xiangshui Miao, Yan Liu*, Yue Hao, Genquan Han and Qihua Xiong

Citation: Liu H, Huang HY, Yu H et al. Vacancy oscillating mode in amorphous binary oxide film by terahertz time domain spectroscopy. *Opto-Electron Adv* **9**, 250217 (2026).

https://doi.org/10.29026/oea.2026.250217

Received: 21 August 2025; Accepted: 9 February 2026; Published online: 31 March 2026

OEA | Opto-Electronic Advances

Article

June 2026, Vol. 9, No. 6

Open Access

Vacancy oscillating mode in amorphous binary oxide film by terahertz time domain spectroscopy

Huan Liu[1,2†], Haiyun Huang[3†], Heng Yu[4], Zhi Gong[6], Fei Yu[2], Zheng Zhang[2], Zhiyong Tan[5], Juncheng Cao[5], Haiyun Liu[3*], Kan-Hao Xue[4*], Xiangshui Miao[4], Yan Liu[1,2*], Yue Hao[2], Genquan Han[1,2] and Qihua Xiong[3]

Abstract: Unveiling the vacancy oscillation mode in amorphous binary oxides films at nanoscale and its impact on ionic conductivity and conductivity spectra is vital to explore the tightly intertwined connection between reversible oxygen migration and stabilizing and controlling the ferroelectric behavior, to complement traditional ferroelectric doped-HfO_2 materials. Using terahertz time-domain spectroscopy (THz-TDS), infrared reflection spectra, and density functional theory (DFT) calculations, we investigate the optical absorption and reflection spectra of crystalline and amorphous ZrO_2 thin film by varying oxygen vacancy concentrations. Experimental results show that oxygen vacancy migration rather than intrinsic paraelectric nature in films significantly affect the conductivity and polarization behavior of ZrO_2 thin film. Notably, except for the phonon modes induce distinct absorption peaks around 11 THz, additional absorption peaks are observed in the 1–2 THz range, which are caused by localized states originated from the oxygen vacancies, supported by DFT calculations. Temperature-dependent ion migration behavior further confirms the role of vacancy oscillation modes in ionic conductivity. DFT calculations additionally reveal how oxygen vacancies alter infrared absorption and optical modes, leading to a redshift in existing absorption peaks or the introduction of new peaks. Our findings unambiguously clarify the oxygen voltammetry characteristics in amorphous ferroelectric binary oxides films. Furthermore, the strategic deployment of amorphous binary oxides films enables the use of low-temperature atomic layer deposition (ALD) growing process, effectively alleviating routing congestion of ferroelectric oxides and offering additional design flexibility for future memory devices with ultra-low effective oxide thickness (EOT) and low thermal budget, and providing alternative technological routes that are poised to propel the development of next-generation more compact ferroelectric devices for advanced process nodes.

Keywords: amorphous binary oxide; ferroelectric material; terahertz time domain spectroscopy; memory

DOI: 10.29026/oea.2026.250217 | CSTR: 32247.14.oea.2026.250217

Citation: Liu H, Huang HY, Yu H et al. Vacancy oscillating mode in amorphous binary oxide film by terahertz time domain spectroscopy. *Opto-Electron Adv* **9**, 250217 (2026).

1 Introduction

Low power nonvolatile memories exhibit switchable and reliable electrical performance, and reignite rejuvenated technological interest for a myriad of applications, notably in big data, artificial intelligence, and cloud computing towards novel computing paradigms at the architecture level especially required for mass data processing[1–3]. Among the current mainstream charge-based memory, ferroelectric random access memory (FeRAM)[4] and resistive switching random access memories (RRAM)[5,6] have emerged as promising candidates for those evolving technologies. Limited to the compatibility with the back end of the traditional complementary metal-oxide-semiconductor (CMOS)

Received: 21 August 2025

Accepted: 9 February 2026

Published online: 31 March 2026

[1]Hangzhou Institute of Technology, Xidian University, Hangzhou 311231, China; [2]Faculty of Integrated Circuits, Xidian University, Xi'an 710071, China; [3]Beijing Academy of Quantum Information Sciences, Beijing 100193, China; [4]School of Integrated Circuits, Huazhong University of Science and Technology, Wuhan 430074, China; [5]State Key Laboratory of Materials for Integrated Circuits, Shanghai Institute of Microsystem and Information Technology, Chinese Academy of Sciences, 865 Changning Road, Shanghai 200050, China; [6]Electrical Engineering College, Zhejiang University, Hangzhou 310027, China.

†These authors contributed equally to this work.

*Correspondence: HY Liu, E-mail: liuhy@baqis.ac.cn; KH Xue, E-mail: xkh@hust.edu.cn; Y Liu, E-mail: xdliuyan@xidian.edu.cn

process, the bistable nature of ferroelectrics and the formation/rupture of conductive filaments stimulated further exploration to a simple binary structured oxide[7]. Among these critical binary oxide materials including ZrO_2, HfO_2, TiO_2, AlO_x, SiO_2, etc., as well-known high-k oxide dielectric material, hafnium oxide (HfO_2) and zirconium oxide (ZrO_2) thin film have attracted more and more attention due to their excellent scalability and compatibility with existing CMOS frameworks, which have been convinced to possess ferroelectric properties and resistive switching[8,9]. Various investigations have been seeking the essential enabler-oxygen vacancy in these mechanisms and finally involved in a similar discipline[10], all converging on a microscopic oxygen-deficient phase, which has been intrinsic in the deposition process of these polycrystalline or amorphous binary oxide films[11,12]. Analogous to the oxide memristor mechanism no doubt induced by oxygen vacancy conduction, vibrant ferroelectric research also indicated that oxygen vacancy along with localized dipoles has a decisive effect on the relative phase stability, which contribute to a stable ferroelectric phase, such as metastable polar orthorhombic phase[13], monoclinic phase in oxygen-deficient HfO_2[11] and rhombohedral phase in Hf(Zr)-excess $Hf(Zr)_{1+x}O_2$[14], induced as well as by the epitaxial strain[15]. In addition, it has long been a consensus among the above different opinions that the ferroelectric properties, especially the polarization switching behaviors and wake-up or fatigue effect, has been unmistakably intertwined with the distribution and the dynamic behavior of oxygen vacancy under an applied electric field[16,17]. Armed with the common understanding of oxygen voltammetry, the emergent research about tunneling junction and resistive memory[18] lay a deep implication of the synergetic effect between resistive switching mechanism and polar switching mechanism[19], which was explained as two coexisting reversible interplay switching mechanisms in a single capacitor cell[12,20]. Some possible postulations have been proposed to explain the intrinsic mechanism[11,21], which still remain no consensus and elusive.

On the other side of on-going miniaturization efforts, as technology scaling approaches its physical limits beyond the 5 nm technology node, the continuous shrinking of device sizes has encountered several overwhelming challenges, including current leakage, increased power consumption, and insufficient electrostatic control, declining reliability, and difficulties in scaling the equivalent oxide thickness (EOT). To further facilitate aggressive transistor scaling, the ongoing miniaturizing ferroelectric film approaching atomic scale becomes a more knotty problem especially in advanced technology nodes, due to enhanced depolarization fields and reduced reliability at nanoscale sizes. Therefore, developing nonvolatile devices with novel operation principles, compact structures and new nanoscale material has been a fundamental solution to achieve faster and denser nonvolatile memory to meet the recurrent requirement of the era of big date storage. Apart from the traditional perovskite ferroelectric oxide which fails to demonstrate polarization switching at atomic scale, polycrystalline hafnia-based ferroelectrics has remained counterintuitively robust ferroelectricity even down to a thickness of one nanometer under a rapid post-metal annealing at 500 °C[22], which impels to a conclusion that hafnia-based ferroelectrics is an apparently distinct mechanism without ferroelectric critical thickness and domain wall growth. Recent studies have revealed new mechanisms for the emergence of ferroelectricity in amorphous ZrO_2 thin film as thin as 5 Å (1 Å =10^{-10} m) or 1 nm, which can be potentially attributed to an amorphous phase fraction expected in such ultrathin films deposited at low temperature (300 °C)[22]. Our previous research indicated that the reversible motion of oxygen ions is the most critical factor involving ferroelectric behavior in these amorphous or polycrystalline binary oxide film with a thickness range of 2.5–3.6 nm with or without high-temperature annealing process for crystallization, such as ZrO_2, HfO_2, AlO_x, and SiO_2, etc., which have been verified to exhibit ferroelectric hysteresis behavior due to oxygen voltammetry[23–26]. To sum up, the use of low-temperature atomic layer deposition (ALD) technology in low-oxygen environments has shown a novel strategy for growing ferroelectric material within polycrystalline and amorphous binary oxide films. To disentangle the classical understanding of polycrystalline HfO_2-based ferroelectricity, we challenge the common belief that a ferroelectric structural constraint mechanism of stabilizing the metastable phase is necessary in these numerous critical binary oxide materials and navigate to another more decisive element of oxygen vacancy voltammetry contributing to ferroelectricity[27].

It remains fundamentally challenging to observe the oxygen vacancy at the atomic scale and their evolution, particularly under the operando conditions during polarization switching or resistive switching. For instance, atomic scale electron microscopy has been adopted to directly image oxygen atoms, which have been constrained within the capacitor stacks grown by epitaxy techniques. Recently, THz conductivity measurements have become essential tools for analyzing carrier transport in solids, for instance, high spatio-temporal resolution in THz-TDS measurements, have been developed to study ion transport in solid electrolytes[28].

Here we demonstrate the vacancy oscillation mode in amorphous ZrO_2 film by time-domain spectroscopy (THz-TDS), exploring its significance in ionic conductivity. By analyzing ion migration temperature-dependent behavior in ultrathin amorphous or crystalline ZrO_2 thin films with different oxygen vacancy concentration, the role of vacancy oscillation modes in ionic conductivity has been investigated and further confirmed. Our investigations further provide more profound understanding of the carrier motion characteristics within unconventional ferroelectric phenomena at the 2D limit in binary oxides films and opens up possibilities towards integration into future highly scaled next-generation silicon electronics.

2 Results and discussions

2.1 Ferroelectric performance of TaN/ZrO_2/TaN capacitors

To investigate the effect of oxygen vacancy migration on the ferroelectric properties of amorphous and crystalline zirconia thin films, we fabricated the TaN/ZrO_2/TaN capacitors with different oxygen vacancy concentrations, as shown in Fig. 1(a). A schematic of the ALD growth principle for ZrO_2 thin film is depicted in Fig. 1(b). In this approach, the oxygen precursor source, H_2O, was pulsed for varying pulse durations during ALD, with three specific pulse times of 0.1 s, 0.2 s, and 0.3 s, to effectively modulate the oxygen vacancy concentration in ZrO_2 thin film. The transmission electron microscopy (TEM) and energy dispersive X-ray spectroscopy (EDS) results for the three devices with different oxygen concentrations are shown in Fig. 1(c). It is evident that the ZrO_2 thin film are in an amorphous state, with a thickness of 12 nm. The corresponding oxygen percentages for O pulsing times of 0.1 s, 0.2 s, and 0.3 s are 56.76%, 59.78%, and 63.66%, respectively. As the O pulsing time decreases, the ZrO_2 thin film become more oxygen-deficient. Fig.1(e–g) show the polarization-voltage (*P-V*) curves at 1 kHz for the TaN/a-ZrO_2/TaN capacitors with O

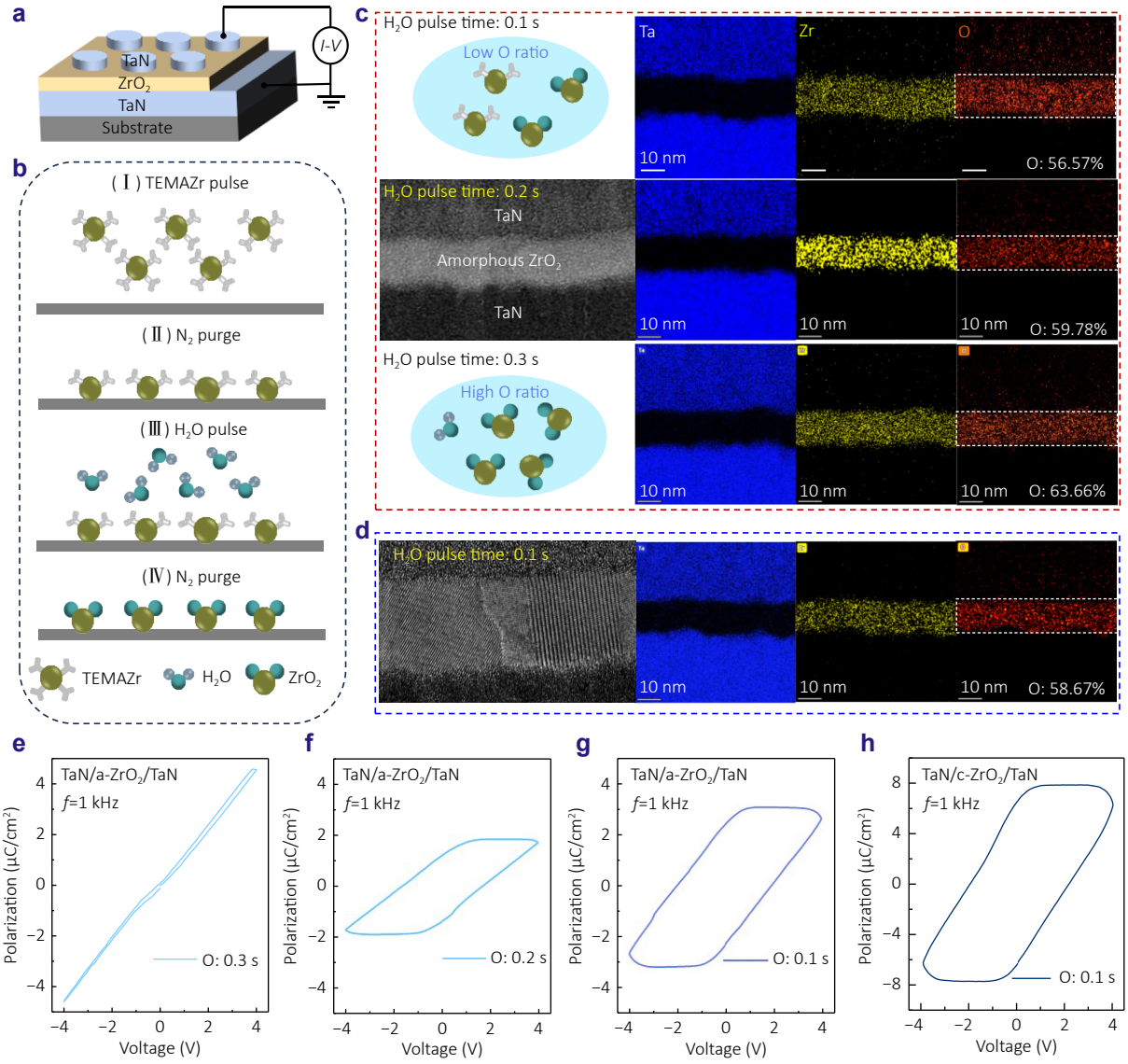

Fig. 1 | Structure and *P-V* performance of the TaN/ZrO_2/TaN capacitors. (a) Schematic illustration of the TaN/ZrO_2/TaN device structure. (b) Reaction mechanism of atomic layer deposition of zirconium oxide using zirconium precursors. (c) HRTEM images of fabricated TaN/ZrO_2/TaN showing the amorphous ZrO_2 film thickness of 12 nm. The corresponding EDX mapping profile analysis results for Zr, O, and Ta. (d) HRTEM images and EDX mapping of fabricated crystallized ZrO_2 device. Measured polarization versus voltage curves at 1 kHz for TaN/a-ZrO_2/TaN capacitors with O pulse time of (e) 0.3 s, (f) 0.2 s, (g) 0.1 s. (h) *P-V* curves for TaN/c-ZrO_2/TaN capacitors with O pulse time of 0.1 s.

pulsing times of 0.3 s, 0.2 s, and 0.1 s, respectively. A transition from paraelectric to ferroelectric-like behavior is observed in the *P*-*V* characteristics of the TaN/a-ZrO_2/TaN capacitors. Notably, as the O pulsing time decreases from 0.3 s to 0.2 s, ferroelectric-like behavior begins to emerge in the system. The remanent polarization (P_r) of this stack further increases when the O pulsing time is reduced to 0.1 s. This suggests that the ferroelectric-like behavior in this structure is related to the formation of an oxygen-deficient layer. On the other hand, for the sample with an O pulsing time of 0.1 s, we also performed *P*-*V* testing on crystallized ZrO_2 samples, as shown in Fig. 1(h), which exhibited similar ferroelectric-like behavior with a higher P_r. The corresponding *I*–*V* characteristics, measured simultaneously with the *P*–*V* loops in Fig. 1(h), is provided in Supplementary Fig. S1. The TEM and EDS results for these samples are shown in Fig. 1(d), where a distinct polycrystalline structure is observed. Distinct lattice fringes were observed in the ZrO_2 film, revealing variations in interplanar spacing, as shown in Supplementary Fig. S2. Measurements identified two sets of lattice fringes with different spacings: 2.63 Å (m-ZrO_2) and 2.98 Å (t-ZrO_2). These correspond to the (200) and (001) planes of m-ZrO_2, as well as the (101) and (110) planes of t-ZrO_2, respectively. Compared to amorphous ZrO_2 samples, the crystallized ZrO_2 film demonstrates a higher oxygen concentration. This can be attributed to the high-temperature annealing process, which improves the lattice structure and reduces oxygen vacancies.

2.2 THz-TDS measurements with the role of oxygen vacancies

As evidenced by our previous study, the amorphous or polycrystalline structure of zirconia has little influence on the validation of ferroelectricity, which makes the high-temperature crystallization process unnecessary, to a lesser extent[23–26]. Due to the metastable nature of amorphous zirconia, the structure of oxygen deficient amorphous zirconia film is routinely alleged to be illusive and invisible due to the absence of long-range order and variations in local order, which can only be evidenced in crystalline structures by conventional material characterization means or be quantitatively described by computational methods. The fundamental questions whether the models or material characterization of oxygen vacancy modulate phonon vibration in crystals can be directly transfer to amorphous, still remain unsolved and debated. This requires a method capable of measuring or characterizing the conductivity of zirconia. THz-TDS, as a way to detect carrier transport in materials, has been widely applied[28–30]. The interaction of THz radiation with matter provides a vital low-energy probe of lattice vibrations, localized defect states, and charge-carrier dynamics, which make the analogy from crystal to amorphous and experimental evidence of the effect of oxygen vacancy in amorphous system become valid.

Figure 2 explores the THz-TDS response of ZrO_2 thin films under different temperatures, providing important insights into the role of oxygen vacancies in electronic and ionic conduction. The details of our experimental setup for the THz-TDS are described in the *Method* and Supplementary information of Fig. S3. Ferroelectric TaN/ZrO_2/TaN MIM capacitors were fabricated on sapphire substrates as sample, which facilitate THz measurements without influencing the ferroelectric properties of the TaN/ZrO_2/TaN structure. The size of each sample is 5 mm × 5 mm. ZrO_2 was prepared in both amorphous and crystalline phases. TaN were fabricated on sapphire substrates of the same thickness as a reference. The sapphire substrates used for the THz measurements are single-crystalline *c*-plane sapphire with a crystallographic orientation of (0001), a thickness of 500 μm, and an optically isotropic cutting configuration. In THz-TDS measurement, we can obtain time domain spectrum of the THz pulse transmitting through the sample $E_s(t)$ and the reference $E_r(t)$. The electric fields $\widetilde{E}_s(\omega)$ and $\widetilde{E}_r(\omega)$ are obtained by FFT of the time domain signal, and the complex transmittance $\widetilde{t}(\omega)$ can be obtained by a ratio

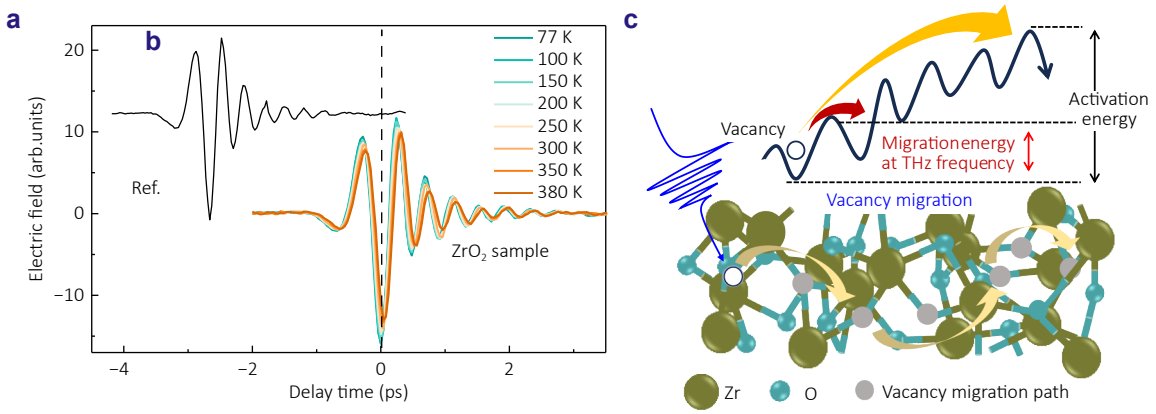

Fig. 2 | THz-TDS measurements in TaN/ZrO_2/TaN. (a) The THz time domain spectroscopy of the sample at different temperatures. (b) The THz time domain spectroscopy of the reference sample at room temperature. (c) The transport mechanism of oxygen vacancies at THz energy levels.

between $\widetilde{E}_s(\omega)$ and $\widetilde{E}_r(\omega)$ (details are given in Supplementary information of Section 1). Absorbance is a heavy index to characterize the absorption of the material to THz.

Figure 2(a) shows the THz-TDS of sample measured at temperatures ranging from 77 K to 380 K, while Fig. 2(b) displays the reference signal at room temperature, offset for better visualization. The schematic diagram of THz spectral processing for the sample and the reference is presented in Supplementary Fig. S4. Compared to the reference, the sample exhibit a noticeable reduction in signal amplitude. Indicating significant absorption and dispersion effects caused by the material's lattice properties and defect states[31,32]. As the temperature increases, the amplitude of the transmitted THz signal decreases, indicating stronger absorption, which is due to increased interactions between THz waves and defect-related localized states, particularly those formed by oxygen vacancies[28,33,34]. Doping elements in ZrO_2 (such as Y, Ce.) can change the lattice structure and vibration mode of ZrO_2, resulting in new absorption in the THz band[35,36]. The absorption frequencies and intensities depend on the lattice vibration mode, the electronic structure, and the presence of defects and impurities[37–45]. Previous studies have shown that sapphire exhibits only a smooth, continuous intrinsic absorption background in the THz frequency range, without localized characteristic absorption features, even at elevated temperatures[46]. Consistent with these reports, our independent measurements of bare sapphire substrates and reference reveal no discernible absorption peaks. Therefore, the characteristic absorbance obtained after background subtraction can be reasonably attributed to the ZrO_2 thin films. Defects such as oxygen vacancy in ZrO_2 can cause local vibration patterns that may produce additional absorption in the THz band[28,33,34,47]. As illustrated in Fig. 2(c), oxygen vacancies generate localized states within the band gap, which lie between the maximum valence band (VBM) and the minimum conduction band (CBM). When exposed to THz radiation, these localized states allow ions to absorb THz energy and undergo transitions. The THz-TDS allows us to investigate the microscopic potential named migration energy in the ZrO_2 thin film, which is involved in the hopping process usually in the range of few meV[28]. Usually, the conduction of oxygen ions in ZrO_2 electrolyte is mainly achieved through the vacancy diffusion mechanism. Ion doping (such as Y_2O_3 doping to form YSZ) or ALD processes can introduce high-concentration oxygen vacancies into the lattice, which act as mediators for the migration of oxygen ions (O^{2-}). Driven by an external electric field or chemical potential gradient, adjacent Oxygen ion overcomes the energy barrier and transition to nearby vacancies, achieving long-range migration through continuous directional exchange and forming an ion current. This is ion conduction and its conductivity efficiency is mainly determined by the oxygen vacancy concentration and the ion migration barrier.

2.3 Absorption spectra analysis

Figure 3 shows the temperature-dependent THz absorbance spectra for crystalline and amorphous ZrO_2 thin films with varying oxygen concentrations. The crystalline ZrO_2 samples with low (D1) and high (D2) oxygen concentrations are shown in Fig. 3(a), while the amorphous ZrO_2 samples with low (C1) and high (C2) oxygen concentrations are shown in Fig. 3(b). The absorption is caused by ion transitions between the localized states introduced by oxygen vacancies. Interestingly, the observed absorption in the 1–2.5 THz range cannot be explained by phonon modes, as earlier studies have shown no phonon contributions in this range for ZrO_2[31,48–50]. For the low oxygen concentration sample (D1), absorption peaks were observed at 1.2 THz and 2.1 THz below room temperature. These peaks remained fixed at low temperatures (77–300 K), but blue-shifted as the temperature increased beyond 300 K. This shift is attributed to enhanced thermal energy, which makes the migration of ions easier, promoting the transition of ions to higher energy levels in the local energy state associated with oxygen vacancies, and causing the absorption peak to shift towards the high-frequency direction. This type of transition is essentially thermally activated. As the temperature rises, the enhanced thermal energy promotes ions to absorb higher-energy THz to complete their migration, strengthening the coupling effect between oxygen vacancies and THz waves, thereby broadening the conductivity spectrum and enhancing the low-frequency absorption response[51,52]. For the high oxygen concentration sample (D2), absorption peaks were broader and located between 1.2 THz and 1.6 THz at low temperatures. However, with increasing temperature, the peaks disappeared completely. This suggests that in high oxygen concentration crystalline samples, fewer oxygen vacancies remain available for ion transitions, leading to weaker absorption at higher temperatures. For the low oxygen concentration amorphous sample (C1), similar to the crystalline D1 sample, absorption peaks were observed at 1.2 THz and 2.1 THz below room temperature. These peaks also exhibited a blue shift as the temperature increased beyond 300 K. However, for the high oxygen concentration amorphous sample (C2), the absorption peak shifted to 1.5 THz at low temperatures and also blue shifted with increasing temperature. Unlike the crystalline samples, the amorphous samples retained more pronounced absorption peaks at higher temperatures. This behavior is attributed to the disordered nature of the amorphous structure, which allows for a broader distribution of oxygen vacancy-related localized states.

The V_O configuration in the ZrO_2 grain was further analyzed using atomically resolved STEM-iDPC imaging (Fig. 3(c–f)). In HAADF images, in which Zr atomic columns appear as the brightest spots, while interstitial oxygen columns remain undetectable due to their weak electron scattering. However, oxygen columns can be observed

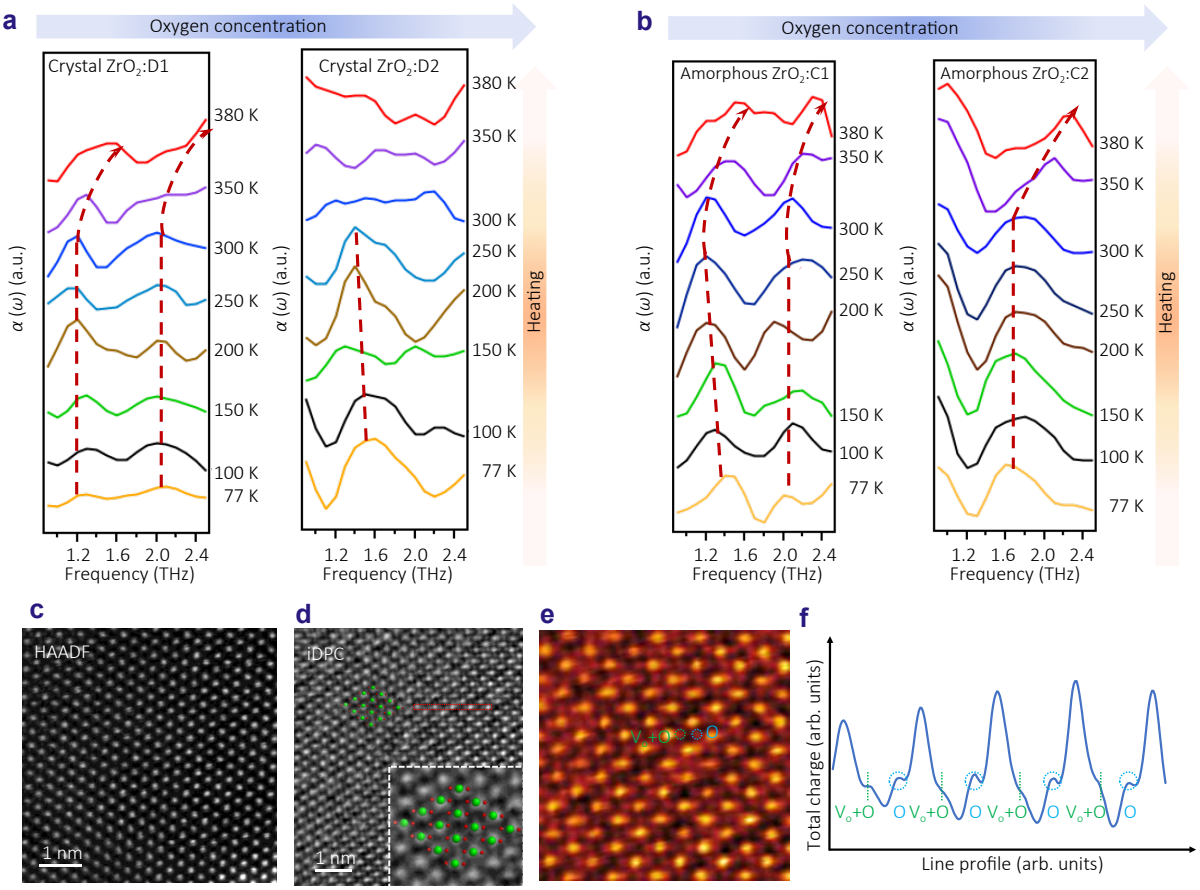

Fig. 3 | THz-TDS measurements with various oxygen concentration. (a) Temperature-dependent absorption peak behavior for crystalline zirconia samples D1 (low oxygen concentration) and D2 (high oxygen concentration). (b) Temperature-dependent absorption peak behavior for amorphous zirconia samples C1 (low oxygen concentration) and C2 (high oxygen concentration). (c) Experimentally acquired HAADF image of the middle parts of ZrO_2 film in samples D1. (d) Filtered iDPC image with inverted contrast, in which the interstitial oxygen columns can be visible. (e) Enlarged views of the columns taken from (c), in which the false-colored image intensity changes to some dotlike rather taillike ones at the oxygen-deficient sites. (f) Results of the line profile taken along corresponding regions highlighted with dashed lines and solid lines in (c), in which the periodic variation of charge density at the anionic sites can be clearly seen.

alongside Zr in the iDPC images. To locate the ordered V_O sites more clearly, an enlarged charge density map was examined. The map shows that the charge intensity at oxygen-deficient sites changes from a "taillike" to a "dotlike" appearance. This indicates localized ions at interstitial columns in sample D1. Line profiles of charge density across interstitial planes in the ZrO_2 film of sample D1 provide further evidence. A periodic variation in charge density at the anionic sites is clearly observed in the crystallized ZrO_2. Localized states induced by oxygen vacancies are distributed between the valence and conduction bands, forming discrete energy levels. Ion transitions between these states require overcoming an migration energy, which is close to the energy barrier required for oxygen vacancy movement as the cause of imprint within the hafnia-zirconia-based material system[53]. At temperatures above 300 K, ion gain enough thermal energy to overcome the migration energy barrier, enabling transitions to higher localized states. Compared to crystalline samples, the localized states in amorphous samples are more disordered, with a broader range of characteristic frequencies, resulting in more pronounced absorption peaks compared to crystalline samples[54]. For more concentrated crystalline (D3) samples, detailed in the Supplementary Fig. S5, the absorption peaks disappeared at both high and low temperatures in crystalline samples. This verifies that excess oxygen reduces vacancy availability.

2.4 Infrared reflection spectra and DFT calculations

The infrared reflection spectra of TaN/a-ZrO_2/TaN and TaN/c-ZrO_2/TaN structures were measured using a Bruker IFS-113V Fourier spectrometer in the spectral range of 1.5-20 THz at 295 K with a resolution of 1 cm^{-1}. Significant enhancement in reflectance was observed in the samples containing ZrO_2 dielectric layers compared to the reference structure, which lacks ZrO_2 dielectric layer. This increase in

reflectance can be attributed to the high dielectric constant of ZrO_2, which introduces strong polarization and optical phonon modes, particularly in the high-frequency range. The crystalline ZrO_2 (c-ZrO_2) layer exhibited sharper and more pronounced phonon-related peaks at 11 THz and 16 THz without any other peaks at low frequency, while the amorphous ZrO_2 (a-ZrO_2) layer showed slightly lower peaks due to the structural disorder and higher defect density. Due to the lack of long-range order characteristic of amorphous structure, modelling oxygen vacancy in amorphous solids has been often carried out by analogy with their crystalline counterparts[55]. We also performed density functional theory (DFT) calculations to simulate the mid-infrared absorption spectra of crystalline ZrO_2 thin films. Calculated IR-active phonon frequencies is shown in Supplementary Table S1. The results reveal that phonon modes induce distinct absorption peaks around 11 THz (Fig. 4(a)), in alignment with experimental measurements and pervious literature reports[49,56,57]. The high-frequency nature of these peaks can be attributed to the stiff bonding environment and transverse polarization characteristics of transverse optical (TO) modes. Specifically, in the pristine ZrO_2 lattice, the TO modes near the Γ point exhibit atomic vibrations perpendicular to the wave vector direction, which generate dipole moments detectable in the infrared spectra. Notably, the simulated mid-infrared absorption spectra also show no absorption peaks in the 1–2.5 THz range (Fig. 4(b)), further confirming that the experimentally observed peaks in the 1–2 THz range are caused by oxygen vacancies rather than intrinsic phonon modes. Additionally, DFT simulations of ZrO_2 with various oxygen concentrations (Fig. 4(c, d)) demonstrate that oxygen vacancies introduce defects that may lead to additional absorption peaks or cause existing absorption peaks to redshift. The two distinct absorption peaks observed at 9.42 THz and 10.59 THz exhibit progressive spectral overlap with increasing oxygen vacancy concentration. This is because the absorption peak, which was originally covered at 10.59 THz, undergoes a redshift, resulting in spectral overlap. This behavior arises from vacancy-induced local lattice distortions, which soften the vibrational force constants of Zr-O bonds and reduce the restoring forces. As oxygen vacancies proliferate, the symmetry-breaking effects and enhanced anharmonic interactions lead to mode coupling between the originally independent peaks. This redshift-overlap trend underscores the critical role of oxygen vacancies in modulating lattice

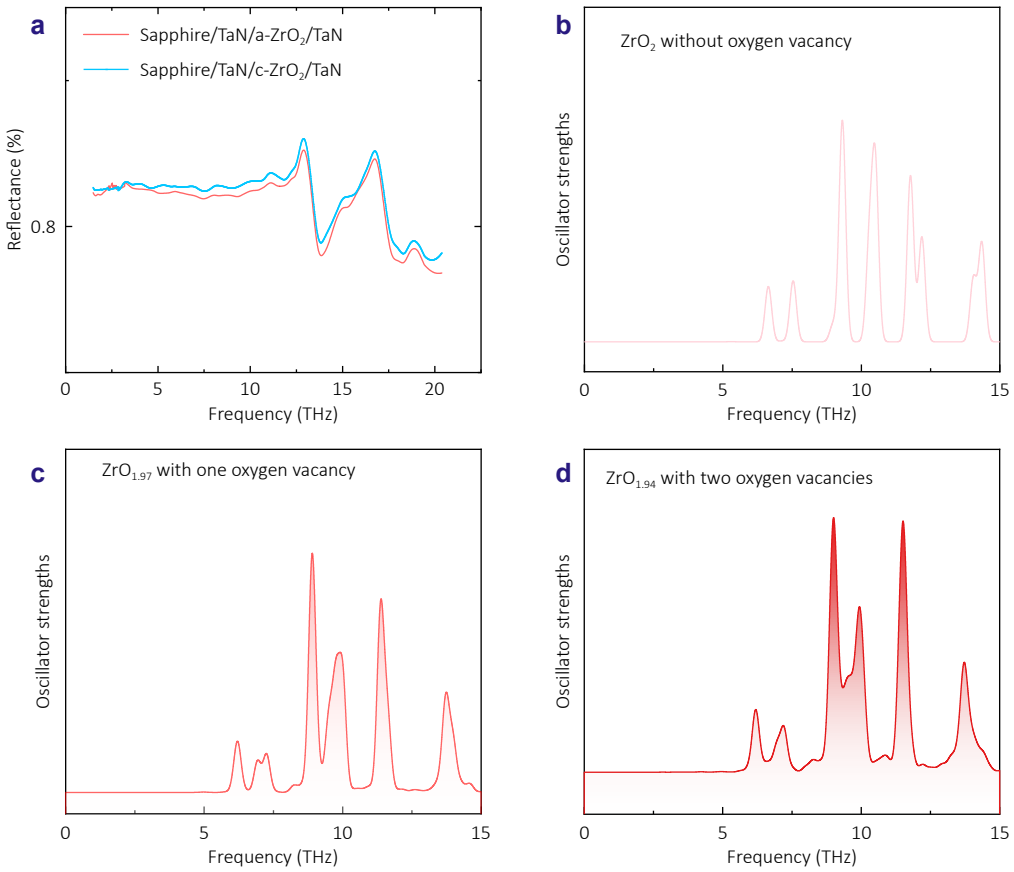

Fig. 4 | Infrared reflection spectra and DFT calculations. (a) The infrared reflection spectra of TaN/a-ZrO_2/TaN and TaN/c-ZrO_2/TaN structures. (b) Simulated the mid-infrared absorption spectra of ZrO_2 thin films by DFT calculations. (c) Infrared spectrum of $ZrO_{1.97}$ ($Zr_{32}O_{63}$) containing one oxygen vacancy. (d) Infrared spectrum of $ZrO_{1.94}$ ($Zr_{32}O_{62}$) containing two oxygen vacancies.

dynamics and infrared response. However, excessive vacancies may lead to phonon scattering and degraded thermal conductivity, necessitating a balance between defect engineering and lattice stability. The supercell models of oxygen vacancies with different coordination numbers and their corresponding infrared spectra are shown in Supplementary Fig. S6. The infrared absorption spectra of these two types of oxygen vacancies are essentially identical.

The relationship between oxygen vacancies and ionic conductivity in (*Y*)-doped bulk ZrO_2 crystals has been widely reported[28,58–63]. In bulk ZrO_2 electrolytes, ionic conductivity is typically measured via low-frequency impedance spectroscopy (< MHz), which only obtain the total activation energy reflecting long-range potential. This activation energy includes the binding energy and migration energy. Traditional low-frequency impedance measurement cannot distinguish the local vibration before ion transition at the microscopic level from the actual transition process, and lacks direct data on migration energy. The microscopic potential of bulk ZrO_2[28] in oxide ion conductors has been reported by THz-TDS measurements, but the test frequency is less than 1 THz[28]; In contrast, our work employs THz-TDS to study ultrathin ZrO_2 films and reveals absorption features in the 1–2.5 THz range that can be directly attributed to oxygen-ion transition. DFT calculations confirm that this frequency range is essentially free from phonon contributions, indicating that the observed peaks to serve as a direct spectroscopic signature of microscopic migration energies. Experimentally, ZrO_2 films with higher oxygen-vacancy concentrations exhibit stronger absorption peaks and, in some cases, dual peaks, while ZrO_2 films with lower vacancy densities show weaker features, demonstrating a clear correlation between ionic transitions and vacancy density. Increasing temperature enhances the absorption intensity and induces a blue shift, reflecting increased ionic oscillation amplitude and transition energy. Structurally, amorphous ZrO_2 films under high-temperature and low-vacancy conditions display stronger ionic transitions than crystalline films, indicating that the disordered structure can maintain accessible vacancies and facilitate microscopic ionic transport. Overall, THz spectroscopy captures the microscopic vibrational dynamics, reveal the synergistic effects of oxygen vacancies, temperature and structural states on ion transitions. It provides information that cannot be directly obtained through traditional bulk phase measurements, highlighting the unique insights of our study into nanoscale ionic dynamics in oxide thin films.

3 Conclusion

In summary, this study reveals the role of vacancy oscillation modes in amorphous ZrO_2 films and their impact on ionic conductivity and optical properties. Through THz-TDS, infrared absorption spectra, and DFT simulations, we show how oxygen vacancies influence absorption characteristics of ZrO_2 films. Oxygen vacancies induce localized states, altering the electrical behavior of the material, especially in the 1–2 THz range where specific absorption peaks appear. These results confirm the significant role of oxygen vacancies in the ionic conductivity of ZrO_2 films. As oxygen vacancy concentration changes, which affects the optical and electrical behavior of the films, particularly in the amorphous samples where the disorder in structure leads to more pronounced effects at higher temperatures. These insights provide a robust foundation for future nonvolatile memory advancement, which involves challenges of integrating low-temperature deposition process for back end of line (BEOL) to unleash the potential of amorphous binary oxides and fully realize its capabilities.

4 Method

Sample fabrication. For electrical measurements, the TaN/ZrO_2/TaN metal-insulator-metal (MIM) capacitors are fabricated on heavily doped p-type silicon substrates (resistivity≈0.02 Ω·cm). After slicing and pre-cleaning, the bottom electrode of 80 nm-thick TaN were deposition by reactive sputtering. Here, to favor the formation of the TaO_xN_y interfacial layer (IL), the pressure and flow of N_2 have been adjusted and in-situ oxidation was adopted. The oxygen flow rate was controlled using an optical emission monitoring system. Then, the chips were loaded into a plasma-enhanced atomic layer deposition (PEALD) chamber for 12 nm-thick ZrO_2 dielectric layer deposition. The ZrO_2 thin film was deposited at 280 °C using $Zr[N(CH_3)_2]_4$ and H_2O as precursors of Zr and O, respectively. These binary oxide films were deposited under oxygen-deficient conditions to tune the concentration of oxygen vacancies. Subsequently, the top electrode with thicknesses of 40 nm TaN was deposited using the same process as the bottom electrode. Finally, the fabrication of MIM Capacitors with amorphous ZrO_2 dielectric was completed after the lithography patterning and dry etching process. Further the MIM Capacitor with crystallized ZrO_2 dielectric was obtained after rapid thermal annealing at 500 °C for 30 s.

Characterization. The polarization-voltage (*P-V*), and current-voltage (*I-V*) measurements were carried out by dynamic hysteresis measurement modules using the TF Analyzer 3000. The measurement pulses were all performed at 1 kHz unless otherwise specified. High-Resolution Transmission Electron Microscopy (HRTEM) was performed with FEI Tecnai G2 F20 operated at 200 kV. The energy dispersive X-ray spectroscopy (EDS) measurements were performed using a Thermo Fisher Scientific Spectra 300 transmission electron microscope equipped with a high-sensitivity EDS detector. The experimental conditions were as follows: an accelerating voltage of 300 kV, an estimated probe diameter of ~0.1 nm, and an estimated beam current of ~120 pA. The nominal convergence semi-angle was 25 mrad, and the collection angle ranged from 49 to 200 mrad.

The energy dispersion was set to 0.1 eV per channel, and the energy resolution, determined from the zero-loss peak, was approximately 0.6 eV. To reduce statistical uncertainty, each spectrum was acquired with an accumulated collection time of 60–120 s using multi-frame integration. Quantitative analysis was carried out using ZAF correction, and a stoichiometric ZrO_2 reference standard was employed for calibration. For each sample, EDS measurements were performed at no fewer than five different locations across the film to account for possible spatial inhomogeneity. The oxygen atomic percentages reported in this work represent the mean values, calculated from quantitative STEM-EDS analysis according to the ratio [O]/([Zr]+[O]), where [O] and [Zr] denote the atomic concentrations of oxygen and zirconium, respectively, obtained after ZAF correction. We acknowledge that EDS is generally considered semi-quantitative for light elements such as oxygen, especially in ultrathin films. Taking into account counting statistics, background subtraction, and systematic uncertainties associated with light-element detection, we estimate the overall uncertainty in the measured oxygen atomic percentage to be less than ±3 at.%. The electrical measurements were performed using a Keithley 4200A-SCS semiconductor parameter analyzer in the ambient atmosphere.

THz experimental measurement. In the experiment, the THz radiation is generated *via* optical rectification in a 1 nm thick ZnTe crystal. Fast Fourier Transform (FFT) breaks down a signal into trigonometric components, such as sine and cosine waves. It expresses the signal as a sum of sinusoids. The femtosecond laser used in the experiment has a repetition frequency of 1 kHz providing 35 fs pulses at central wavelength of 800 nm. The 800 nm laser is divided into two beams through the beam splitter, one beam is used to generate THz radiation via a nonresonant optical rectification in a 1-mm-thick <110> ZnTe crystal, and the other beam is used to detect the THz pulses. The generated THz pulses is focused on the sample through an off-axis parabolic mirror, transmitted to the sample, and is collinear with the detection pulse to irradiate the electro-optic ZnTe crystal. Obtaining THz time-domain spectral signals through electro-optic sampling method (Supplementary Fig. S7). The transient THz electric field modulates and changes the birefringence of ZnTe crystals. When the detection pulse passes through the ZnTe crystal with a refractive index change, the polarization state changes. The change in polarization state corresponds to the electric field strength of the THz pulse. By changing the time of the THz pulse relative to the detection pulse through a delay line, a complete THz time-domain spectrum is obtained using a point by point scanning method (Supplementary Fig. S8). The region where the THz beam is generated and detected is placed in a vacuum chamber to reduce the absorption of atmospheric water vapor which allows measurements from 380 K down to 78 K. To properly address the temperature dependence of substrate optical parameters, we independently measured the THz time-domain spectra of sapphire and reference over the entire temperature range used in this work (77–380 K). The temperature-induced variations in the absorbance of reference were quantitatively extracted and subsequently subtracted from the sample spectra. This procedure allows us to isolate the THz response of the ZrO_2 thin films.

Density functional theory (DFT) calculations. DFT calculations were performed within the Vienna ab initio simulation package (VASP) using the projector-augmented wave (PAW) method[64,65]. The valence electron configurations were 2s and 2p for O; 4s, 4p, 4d, and 5s for Zr; The Perdew-Burke-Ernzerhof functional generalized gradient-approximation type (GGA-PBE) was adopted to treat the exchange-correlation. The atomic positions and lattice constants were fully relaxed until the atomic Hellmann-Feynman forces were smaller than 0.001 eV/Å in each direction. The force constants are calculated using the finite difference method. The Born effective charge tensors were calculated using the density functional perturbation theory (DFPT) method. Subsequently, the force constants and dielectric tensors were input into the Phonopy software for post-processing to obtain the infrared spectra[66].

References

1. Ielmini D, Wong HSP. In-memory computing with resistive switching devices. *Nat Electron* **1**, 333–343 (2018).
2. Ambrogio S, Narayanan P, Tsai H et al. Equivalent-accuracy accelerated neural-network training using analogue memory. *Nature* **558**, 60–67 (2018).
3. Rasch MJ, Mackin C, Le Gallo M et al. Hardware-aware training for large-scale and diverse deep learning inference workloads using in-memory computing-based accelerators. *Nat Commun* **14**, 5282 (2023).
4. Hirtzlin T, Bocquet M, Penkovsky B et al. Digital biologically plausible implementation of binarized neural networks with differential hafnium oxide resistive memory arrays. *Front Neurosci* **13**, 1383 (2020).
5. Xue CX, Chiu YC, Liu TW et al. A CMOS-integrated compute-in-memory macro based on resistive random-access memory for AI edge devices. *Nat Electron* **4**, 81–90 (2021).
6. Wan WE, Kubendran R, Schaefer C et al. A compute-in-memory chip based on resistive random-access memory. *Nature* **608**, 504–512 (2022).
7. Schroeder U, Park MH, Mikolajick T et al. The fundamentals and applications of ferroelectric HfO_2. *Nat Rev Mater* **7**, 653–669 (2022).
8. Noheda B, Nukala P, Acuautla M. Lessons from hafnium dioxide-based ferroelectrics. *Nat Mater* **22**, 562–569 (2023).
9. Crema APS, Istrate MC, Silva A et al. Ferroelectric orthorhombic ZrO_2 thin films achieved through nanosecond laser annealing. *Adv Sci* **10**, 2207390 (2023).
10. Zhu TY, Ma LY, Deng SQ et al. Progress in computational understanding of ferroelectric mechanisms in HfO_2. *npj Comput Mater* **10**, 188 (2024).
11. Yu CX, Ma HL, Li MQ et al. Insights into the origin of robust ferroelectricity in HfO_2-based thin films from the order-disorder transition driven by vacancies. *Phys Rev Appl* **22**, 024028 (2024).
12. Cheng Y, Gao ZM, Ye KH et al. Reversible transition between the polar and antipolar phases and its implications for wake-up and fatigue in HfO_2-based ferroelectric thin film. *Nat Commun* **13**, 645

(2022).
13. Zhou C, Ma LY, Feng YP et al. Enhanced polarization switching characteristics of HfO_2 ultrathin films via acceptor-donor co-doping. *Nat Commun* **15**, 2893 (2024).
14. Wang Y, Tao L, Guzman R et al. A stable rhombohedral phase in ferroelectric $Hf(Zr)_{1+x}O_2$ capacitor with ultralow coercive field. *Science* **381**, 558–563 (2023).
15. Qi YB, Singh S, Lau C et al. Stabilization of competing ferroelectric phases of HfO_2 under epitaxial strain. *Phys Rev Lett* **125**, 257603 (2020).
16. Jiang PF, Luo Q, Xu XX et al. Wake-up effect in HfO_2-based ferroelectric films. *Adv Electron Mater* **7**, 2000728 (2021).
17. Chen JJ, Qian HJ, Zhang HR et al. Physical origin of recoverable ferroelectric fatigue and recovery for doped-HfO_2: toward endurance immunity. In *2023 International Electron Devices Meeting (IEDM)* 1–4 (IEEE, 2023). https://doi.org/10.1109/IEDM45741.2023.10413825.
18. Peng HY, Li GP, Ye JY et al. Electrode dependence of resistive switching in Mn-doped ZnO: filamentary versus interfacial mechanisms. *Appl Phys Lett* **96**, 192113 (2010).
19. Zhu ZX, Zhao HY, Wang H et al. Three types of resistive switching in ferroelectric $Hf_{0.5}Zr_{0.5}O_2$ films mediated by polarization reversal and oxygen vacancy migration. *Rare Met* **43**, 6765–6770 (2024).
20. Max B, Pešić M, Slesazeck S et al. Interplay between ferroelectric and resistive switching in doped crystalline HfO_2. *J Appl Phys* **123**, 134102 (2018).
21. Lee HJ, Lee M, Lee K et al. Scale-free ferroelectricity induced by flat phonon bands in HfO_2. *Science* **369**, 1343–1347 (2020).
22. Cheema SS, Shanker N, Wang LC et al. Ultrathin ferroic HfO_2-ZrO_2 superlattice gate stack for advanced transistors. *Nature* **604**, 65–71 (2022).
23. Liu H, Wang CX, Han GQ et al. ZrO_2 ferroelectric FET for non-volatile memory application. *IEEE Electron Device Lett* **40**, 1419–1422 (2019).
24. Peng Y, Xiao WW, Han GQ et al. Memory behavior of an Al_2O_3 gate dielectric non-volatile field-effect transistor. *IEEE Electron Device Lett* **41**, 1340–1343 (2020).
25. Feng Z, Peng Y, Shen Y et al. Ferroelectric-like behavior in TaN/high-k/Si system based on amorphous oxide. *Adv Electron Mater* **7**, 2100414 (2021).
26. Liu H, Peng Y, Han GQ et al. ZrO_2 ferroelectric field-effect transistors enabled by the switchable oxygen vacancy dipoles. *Nanoscale Res Lett* **15**, 120 (2020).
27. Liu H, Yu F, Chen B et al. Evidence for reversible oxygen ion movement during electrical pulsing: enabler of emerging ferroelectricity in binary oxides. *Mater Futures* **3**, 035701 (2024).
28. Morimoto T, Nagai M, Minowa Y et al. Microscopic ion migration in solid electrolytes revealed by terahertz time-domain spectroscopy. *Nat Commun* **10**, 2662 (2019).
29. Beltukov YM, Fusco C, Tanguy A et al. Transverse and longitudinal vibrations in amorphous silicon. *J Phys Conf Ser* **661**, 012056 (2015).
30. Grimsditch M, Polian A, Vogelgesang R. The phonon density of states in amorphous materials. *J Phys Condens Matter* **15**, S2335–S2341 (2003).
31. MacDougall J, Namai A, Jia FD et al. The absorption properties of ZrO_2 nanoparticles in the THz and sub-THz frequency ranges. *RSC Adv* **14**, 7903–7909 (2024).
32. Xu JP, Zhang RJ, Zhang Y et al. The thickness-dependent band gap and defect features of ultrathin ZrO_2 films studied by spectroscopic ellipsometry. *Phys Chem Chem Phys* **18**, 3316–3321 (2016).
33. Hendry E, Koeberg M, O'regan B et al. Local field effects on electron transport in nanostructured TiO_2 revealed by terahertz spectroscopy. *Nano Lett* **6**, 755–759 (2006).
34. Zheng SY, Shi DP, Liu LJ et al. Oxygen vacancy-related dielectric relaxation and electrical conductivity in La-doped $Ba(Zr_{0.9}Ti_{0.1})O_3$ ceramics. *J Mater Sci Mater Electron* **25**, 4058–4065 (2014).
35. Liu T, Zhang XF, Wang XN et al. A review of zirconia-based solid electrolytes. *Ionics* **22**, 2249–2262 (2016).
36. Ostanin S, Salamatov E, Craven AJ et al. Theory of the phases and atomistic structure of yttria-doped zirconia. *Phys Rev B* **66**, 132105 (2002).
37. Ferguson B, Zhang XC. Materials for terahertz science and technology. *Nat Mater* **1**, 26–33 (2002).
38. Kharton VV, Marques FMB, Atkinson A. Transport properties of solid oxide electrolyte ceramics: a brief review. *Solid State Ionics* **174**, 135–149 (2004).
39. Goff JP, Hayes W, Hull S et al. Defect structure of yttria-stabilized zirconia and its influence on the ionic conductivity at elevated temperatures. *Phys Rev B* **59**, 14202–14219 (1999).
40. van Exter M, Fattinger C, Grischkowsky D. Terahertz time-domain spectroscopy of water vapor. *Opt Lett* **14**, 1128–1130 (1989).
41. Kindt JT, Schmuttenmaer CA. Far-infrared dielectric properties of polar liquids probed by femtosecond terahertz pulse spectroscopy. *J Phys Chem* **100**, 10373–10379 (1996).
42. da Silva JH, Lima JA Jr, Freire PTC et al. Raman spectroscopy and inelastic neutron scattering study of crystalline L-valine. *J Phys Condens Matter* **21**, 415404 (2009).
43. Allis DG, Korter TM. Development of computational methodologies for the prediction and analysis of solid-state terahertz spectra. *Int J High Speed Electron Syst* **17**, 193–212 (2007).
44. Nomura K, Ohta H, Takagi A et al. Room-temperature fabrication of transparent flexible thin-film transistors using amorphous oxide semiconductors. *Nature* **432**, 488–492 (2004).
45. Schlichting KW, Padture NP, Klemens PG. Thermal conductivity of dense and porous yttria-stabilized zirconia. *J Mater Sci* **36**, 3003–3010 (2001).
46. Grischkowsky D, Keiding S, van Exter M et al. Far-infrared time-domain spectroscopy with terahertz beams of dielectrics and semiconductors. *J Opt Soc Am B* **7**, 2006–2015 (1990).
47. Dutta G, Hembram KPSS, Rao GM et al. Effects of O vacancies and C doping on dielectric properties of ZrO_2: a first-principles study. *Appl Phys Lett* **89**, 202904 (2006).
48. Li CW, McKerns MM, Fultz B. A Raman spectrometry study of phonon anharmonicity of zirconia at elevated temperatures. *J Am Ceram Soc* **94**, 224–229 (2011).
49. Zhao XY, Vanderbilt D. Phonons and lattice dielectric properties of zirconia. *Phys Rev B* **65**, 075105 (2002).
50. Nagai M, Higashitani Y, Ashida M et al. Terahertz-induced martensitic transformation in partially stabilized zirconia. *Commun Phys* **6**, 88 (2023).
51. Magyari-Köpe B, Park SG, Lee HD et al. First principles calculations of oxygen vacancy-ordering effects in resistance change memory materials incorporating binary transition metal oxides. *J Mater Sci* **47**, 7498–7514 (2012).
52. Wu Y, Shu RW, Zhang JB et al. Oxygen vacancies regulated microwave absorption properties of reduced graphene oxide/multi-walled carbon nanotubes/cerium oxide ternary nanocomposite. *J Alloys Compd* **819**, 152944 (2020).
53. Fengler FPG, Pešić M, Starschich S et al. Domain pinning: comparison of hafnia and PZT based ferroelectrics. *Adv Electron Mater* **3**, 1600505 (2017).
54. Prasai B, Cai B, Underwood MK et al. Properties of amorphous and crystalline titanium dioxide from first principles. *J Mater Sci* **47**, 7515–7521 (2012).
55. Bae J, Kwon C, Park SO et al. Tunable ion energy barrier modulation through aliovalent halide doping for reliable and dynamic memristive neuromorphic systems. *Sci Adv* **10**, eadm7221 (2024).

56. Verdi C, Karsai F, Liu PT et al. Thermal transport and phase transitions of zirconia by on-the-fly machine-learned interatomic potentials. *npj Comput Mater* **7**, 156 (2021).
57. Maczka M, Lutz ETG, Verbeek HJ et al. Spectroscopic studies of dynamically compacted monoclinic ZrO_2. *J Phys Chem Solids* **60**, 1909–1914 (1999).
58. Shin S, Ishigame M. Defect-induced hyper-Raman spectra in cubic zirconia. *Phys Rev B* **34**, 8875–8882 (1986).
59. Garcia-Barriocanal J, Rivera-Calzada A, Varela M et al. Colossal ionic conductivity at interfaces of epitaxial ZrO_2: Y_2O_3/$SrTiO_3$ heterostructures. *Science* **321**, 676–680 (2008).
60. Teranishi T, Hayashi H, Kishimoto A et al. Broadband spectroscopy of the complex conductivity of polycrystalline yttria-stabilized zirconia. *Mater Sci Eng B* **177**, 69–73 (2012).
61. Kilo M, Argirusis C, Borchardt G et al. Oxygen diffusion in yttria stabilised zirconia-experimental results and molecular dynamics calculations. *Phys Chem Chem Phys* **5**, 2219–2224 (2003).
62. Cheikh A, Madani A, Touati A et al. Ionic conductivity of zirconia based ceramics from single crystals to nanostructured polycrystals. *J Eur Ceram Soc* **21**, 1837–1841 (2001).
63. Krishnamurthy R, Srolovitz DJ, Kudin KN et al. Effects of lanthanide dopants on oxygen diffusion in yttria-stabilized zirconia. *J Am Ceram Soc* **88**, 2143–2151 (2005).
64. Kresse G, Furthmüller J. Efficient iterative schemes for *ab initio* total-energy calculations using a plane-wave basis set. *Phys Rev B* **54**, 11169–11186 (1996).
65. Kresse G, Furthmüller J. Efficiency of ab-initio total energy calculations for metals and semiconductors using a plane-wave basis set. *Comput Mater Sci* **6**, 15–50 (1996).
66. Togo A, Tanaka I First principles phonon calculations in materials science. *Scr Mater* **108**, 1–5 (2015).

Acknowledgements

The authors acknowledge support from the National Key Research and Development Project (Grant No. 2023YFB4402303), the National Natural Science Foundation of China (Grant No. 62204226, 62374151, 62574159, 62025402, 62090033 and 92264202), Major Program of Zhejiang Natural Science Foundation (Grant No. DT23F0402).

Author contributions

Y.L., H.L., and K.X. designed the project and guided the research. H.L. and F.Y. fabricated the samples and performed the electrical switching experiments with the help of H.H., F.Y., and Z.Z. H.L performed the TEM experiments and analyzed the data. K.X., and H.Y. performed the ab initio calculations. H.L., H.H., and H.Y. wrote and revised the paper with the help of Y.L. and H.L. All authors contributed to extensive discussions of the results.

Competing interests

The authors declare no competing interests.

Data availability

The data that support the plots within this paper and other findings of this study are available from the corresponding authors upon reasonable request.

Code availability

All code used in this study is available from the corresponding authors upon reasonable request.

Supplementary information

Supplementary information for this paper is available at
https://doi.org/10.29026/oea.2026.250217